Commun.Fac.Sci.Univ.Ank.Series A2-A3
Volume 61, Number 1, Pages 76-101 (2019)
DOI: 10.33769/aupse.547407
ISSN 1303-6009 E-ISSN 2618-6462
http://communications.science.ankara.edu.tr/index.php?series=A2A3

FOCUSING, IMAGING AND FOURIER TRANSFORMING WITH A LARGE NUMERICAL APERTURE, DIELECTRIC FLAT PHOTONIC CRYSTAL LENS IN METAMATERIAL REGIME

EVRIM COLAK, ATILLA OZGUR CAKMAK

Abstract. Traditional Gradient Index Photonic Crystals (GRIN PCs) are designed under the assumption of the paraxial wave approximation and the slowly changing refractive index. In contrast, in this study, an untraditional Gradient Index Photonic Crystal (GRIN PC) is employed within the long wavelength regime to exhibit focusing, imaging and Fourier Transforming. A very large numerical aperture is aimed by breaking both the paraxial wave approximation and the slowly changing refractive index assumption. This untraditional GRIN PC is shown to exhibit very similar lensing characteristics as its analytically solvable traditional counterparts demonstrate. The results suggest that Fourier Transforming together with Fractional Fourier Transforms can be obtained from the present design. The performance of the GRIN PC lens is very much dependent on the excitation source as it is expected from GRIN optics and adiffractional propagating beams over large distances can be obtained.

1. INTRODUCTION

Metamaterials (MTM) have emerged with the promise of building superlenses as early as in 2000s. Such lenses would exceptionally recapture the high spatial frequencies to reconstruct the subwavelength features [1]. There have been several demonstrations of subwavelength focusing [2- 4] and cloaking [5,6] where simultaneous negative dielectric permittivity (ε_r) and magnetic permeability (μ_r) could be observed. The difficulty of obtaining simultaneous negative electromagnetic constitutive parameters with moderate optical losses compelled the researchers to shift to hyperbolic MTMs which are also volumetric, chiral structures and plasmonic counterparts [7-11]. Anisotropic nature of the MTM mimicked the negative refraction for hyperbolic MTMs whereas the bianisotropy helped to relieve the strict requirement (simultaneous negative ε_r and μ_r) on the negative refraction for resonating chiral structures. Plasmonic lenses were found to be the solution to

---

Received by the editors: April 01, 2018; Accepted: May 27, 2019.
Key word and phrases: Graded Index Photonic Crystal (GRIN) lens, Fractional Fourier Transform, Fourier Optics, Adiffractional beam propagation.

reach below 100nm resolution in lithographic methods to be utilized as an active element of the exposure systems [12]. In the following years, metasurfaces specifically metalenses were commonly employed to end up with superior imaging performances that could battle chromatic aberrations, as well [13,14]. Hence, volumetric MTM structures seemingly left their place to wavefront modification based lower dimensional devices.

On the other hand, while still being volumetric, dielectric based Graded Index Photonic Crystals (GRIN PCs) have been proposed in order to build lenses that would be immune to non-idealities stemming from parasitic losses and resonator configurations [15,16]. Since then the GRIN PCs have been efficiently shown to guide the light carefully to serve as waveguide input couplers [17], to slow down the light [18] and to achieve self-collimation, super-bending and mirage effects [19-22]. The main ideas have been borrowed from the already well-established GRIN optics as the lattice configurations have been carefully adjusted to mimic GRIN media [23].

In this study, a PC with a quadratic index profile will be analyzed in depth to illustrate the focusing properties of a full dielectric configuration for a most general case, i.e., outside the constraints of a paraxial approximation and the assumption of a slowly changing index profile. The proposed GRIN PC's imaging performance will be studied while staying inside the metamaterial regime. Metamaterial regime is attributed to be the operating wavelength range where the lattice spacings of the designed PC is much smaller than the incident light's wavelength. The present work will start with the analytical investigation of a perfect lens. The underlying evanescent wave amplification mechanism will be studied with the help of Transfer Matrix Method (TMM). The historical difficulties arising from the creation of such a perfect lens will be presented to the reader and the GRIN PC configuration, which is based on the homogenization methods will be examined. To the best of our knowledge, a prior analysis of the homogenization procedure for PC based GRIN lenses for the most general case without the paraxial wave approximation or the gradual refractive index change have not been carried out before even though several self-focusing (SELFOC) GRIN medium have been thoroughly examined. The present paper serves as a bridge between the GRIN optics and GRIN PCs while adapting the Maxwell-Garnett theory to study the focusing and imaging phenomenon in depth. The paper will attempt to explain ray optics, imaging, Fourier optics, bandwidth management and source dependency of the current GRIN PC by forming links with the well-established GRIN optics.

2. METAMATERIAL BASED DESIGNS

Subwavelength focusing has been accepted as a pioneering accomplishment for possible future applications, especially in the near-field science. The appearance of the negative-index materials (NIM) has escalated the endeavors towards the construction of improved lenses. MTMs and PCs have been the fundamental building blocks of such lensing activities. The main physic entails the negative refraction and evanescent wave amplification.

An evanescent field ($E_{1,2,3}$) propagating along z can be written in three sections (see Fig. 1) separately with the given field coefficients (A, B, C, D and F) based on the standard TMM analysis. $E_1 = Ae^{-k_{1z}z} + Be^{k_{1z}z}$, $E_2 = Ce^{-k_{2z}z} + De^{k_{2z}z}$, $E_3 = Fe^{-k_{3z}z}$, where the wave propagation constants along z-axis are $k_{1z,2z,3z} = \sqrt{k_{1x,2x,3x}^2 - \omega\varepsilon_{1,2,3}\mu_{1,2,3}/c}$ due to the evanescent nature of the field. ω and c are angular frequency and the speed of light, respectively. The detailed discussions and analysis of TMM formalism is given in Chs. 9 and 10 of ref. 24. Hence, applying the boundary conditions dictating that the tangential electric and magnetic fields are to be continuous on both sides at $z = -a$ and $z = a$, after some algebra C and D can be linked to the coefficient F as:

$$2\begin{bmatrix} 1+\frac{k_{2z}}{k_{3z}}\frac{\mu_3}{\mu_2} & 1-\frac{k_{2z}}{k_{3z}}\frac{\mu_3}{\mu_2} \\ 1-\frac{k_{2z}}{k_{3z}}\frac{\mu_3}{\mu_2} & 1+\frac{k_{2z}}{k_{3z}}\frac{\mu_3}{\mu_2} \end{bmatrix}^{-1} \begin{bmatrix} Fe^{-k_{3z}a} \\ 0 \end{bmatrix} = \begin{bmatrix} Ce^{-k_{2z}a} \\ De^{k_{2z}a} \end{bmatrix} \tag{2-1}$$

The remaining parameters (A and B) can also be linked to F and after a renormalization procedure to satisfy the boundary conditions, Fig. 1(a) can be obtained. As it can be clearly seen, the evanescent wave reaching the boundary z=-a is amplified within the normalized wave impedance matched ($Z = \sqrt{\mu_r/\varepsilon_r} = 1$) region. The main difficulty in recreating the subwavelength images stems from the fact that the high spatial frequency components that carry very critical information about the subwavelength image cannot propagate to the far-field. Such components are normally expected to die out as it can be noticed in medium 1 in Fig. 1(a). By employing a 100nm artificial superlens, these high spatial frequency components can have a chance to be recovered as they are amplified to the output plane during their propagation.

In reality, achieving a perfect lens has never been an easy task as the medium also needs to have impedance matched to the air on both sides. As soon as the impedance matching condition is relaxed, the reflections start to appear as it is demonstrated in Fig. 1(b) for two different wave impedance cases. The evanescent amplification is still observed. Figure 2 illustrates a more realistic exemplary negative index lens that consists of a dispersive homogenized medium in order to mimic the characteristics of a MTM. The constitutive parameters of the medium, and thereby the permittivity and permeability of the MTM are assumed to be of the Drude and Lorentz form, respectively. A similar model had earlier been studied at a different frequency in ref. 25 and the Drude/Lorentz description of a double negative MTM is a common approach. The simulations have been carried out in CST Microwave Studio, a commercial software which is based on Finite Integration Technique. Meanwhile, the scalability of the Maxwell's equations allows us to make analogies between the microwave and optical frequency ranges. The absolute values of the electric field distribution maps have been plotted at 17.7 GHz under the illumination of a modeled horn antenna. The launched beam possesses wavefronts with spherical features. The phase advancement is along the propagation direction in free space (at P_1 and P_3), whereas the left handed behavior dictates a negative phase velocity with respect to the group velocity inside the MTM (at P_2). The conservation of the momentum at the air-MTM boundary compels the wave fronts to collapse and the focusing is attained. The beam quickly starts to diverge once it leaves the MTM.

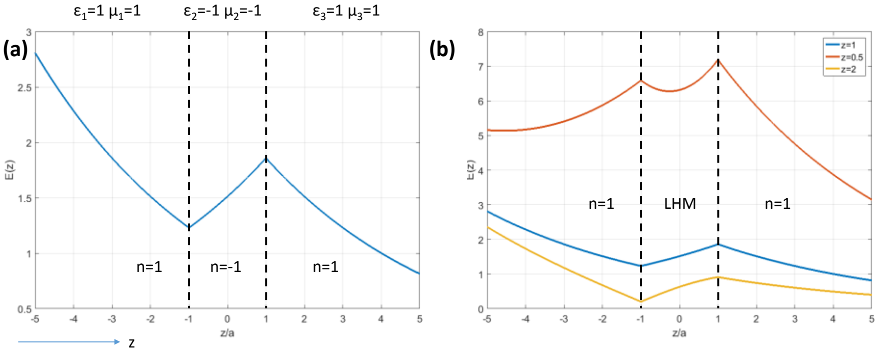

Figure 1. A 100nm thickness left-handed medium (LHM) is sandwiched between two dielectric media along *z*-axis. The evanescent field in medium 1 is launched from the left hand side. The electric fields ($E(z)$) are plotted at 500 THz for (a) wave impedance (Z, normalized by $Z_0 = 120\pi\ \Omega$) matched case; LHM has Z=1 and (b) Z-matched and unmatched cases together. LHM impedance cases: Z=1 (blue), Z=0.5 (red), Z=2 (orange).

The conventional MTM configuration suffers from possible losses which originate from the imaginary parts of the constitutional parameters. The impedance mismatches at the air-MTM interface causes standing waves between the source and the structure. Besides, the planar negative index lenses do not have a definite focal length. The MTM lens could focus the incident beams launched from a source that is 4λ away in Fig. 2, but an object at infinity would not be resolved by the planar MTM lens. Instead, planoconcave NIM lenses are built with PCs [26] and MTMs [27], which can accept wave fronts with larger radius of curvatures. Consequently, a planar GRIN formalism presents itself as a favorable choice in view of the fact that it may avoid the cost and manufacturing complexities that a planoconcave lens brings. Hence, an increasing number of publications have rapidly adapted the GRIN concept for the MTM lenses as well [28-32]. Essentially, the main disadvantage of the MTM based lens is the frequency dependency of the negative refraction mechanism since the double negative behavior can be sustained for a limited operational band. Liu *et al*. had suggested working with non-resonant metamaterials in ref. 33, which radically increased the frequency bandwidth. The broadband MTM based designs have been utilized by relying on the small variations of the design parameters of the unit lattice along the propagation direction, which results in a gradient change of the refractive index to control the light's trajectory.

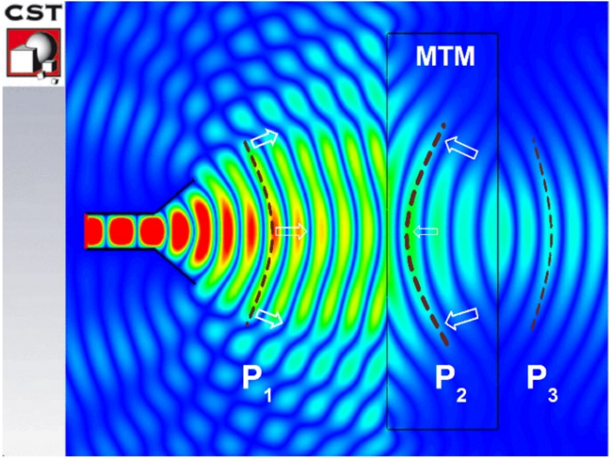

Figure 2. The absolute values of the electric field distributions for a MTM based lens at *f*=17.7 GHz. P_1, P_2 and P_3 signify three different positions along the direction of propagation. The dashed wine-colored curves exhibit the wave fronts roughly at P_1, P_2 and P_3. The excitation source is modeled with a horn antenna on the left hand side of the figure. The white arrows indicate the direction of the wave-vectors on the same wave front. The effective permittivity function is $\varepsilon_{eff}(\omega) = \varepsilon_\infty - \omega_p/[\omega(\omega - i\nu_c)]$ and the effective permeability function is $\mu_{eff}(\omega) = \mu_\infty + (\mu_s - \mu_\infty)\omega_0{}^2/(\omega_0{}^2 + i\omega\delta - \omega^2)$, $\varepsilon_\infty = 1.62$, $\omega_p = 2\pi \times 31$ GHz, $\nu_c = 30.69$ MHz, $\mu_\infty = 1.12$, $\mu_s = 1.26$, $\omega_o = 2\pi \times 17$ GHz, $\delta = 500$ MHz.

In contrast, the GRIN PC already works over a relatively broader frequency region. Given that the lensing effect is based on the phase retardation mechanism owing to the direct lattice spacing modulation, an intuitive examination even at this stage suggests that the GRIN PCs are less sensitive to the frequency variations. Yet, this point is going to be elaborately covered in the succeeding parts.

3. GRIN PC IN METAMATERIAL REGIME

3.1. Design of the GRIN PC and Ray Trajectories:

GRIN PCs have been exploited in the long wavelength regime, for which the effective medium theory holds. Actually, the earliest designs that utilized the effective medium theory within the context of the 1-D GRIN PCs go back to the year 2005. The proposed designs were envisioned to be used in imaging, guiding, mode matching and coupling [34,35]. The GRIN PC has been shown to simultaneously possess the multi-functionality as beam deflectors and beam aperture modifiers [36]. Consequently, waveguide bends [37] and a cylindrical optical black hole with an omnidirectional absorbance [38] have been made available in the following years. Even a free-space carpet cloak has been proposed by making use of the GRIN PCs in metamaterial regime [39]. An extensive study of the possible GRIN PC lenses in metamaterial regime has been carried out in ref. 40 and similar lens design techniques have rapidly been addressed in the literature [41-43].

Accordingly, we have adapted a GRIN PC lens design that is based on the homogenization procedure. The implementation of the homogenization procedure is derived from Maxwell-Garnett theory. The results are presented in Fig. 3. GRIN PC comprises alumina rods ($\varepsilon_{rod} = n_{rod}^2$=9.61) with varying radii. The dispersion graph in Fig. 3(a) indicates the phase difference ($\Delta\varphi$) within the 1st band along the propagation distance ($\Delta\varphi \propto \Delta k$). The phase difference is expected to be accumulated between two sets of rods with different radii (r_1 and r_2). The radius of the rods changes in the transverse direction (x-axis). Then, the refractive index at any point along x-axis is calculated with the formula that is given in the inset of Fig. 3(a). Thus, a quadratic refractive index variation can be sustained for n(x), where f(x)=π r^2⁄a^2 is the filling factor for each unit cell and a is the constant lattice spacing in the transverse direction. As a result of the quadratic variation, a focusing effect is observed at the end of the structure.

The presented lensing will occur due to the wavefront shaping and thereby phase retardation mechanisms. Hence, the phase velocities (v_p) for each lattice point corresponding to the rods with different filling factors need to be calculated to estimate $v_p = \omega/k$. The isofrequency contours (IFCs) are presented in Fig. 3(b), which turn out to be centered around Γ point in the lattice symmetry as already hinted in Fig. 3(a). The IFCs are plotted for the smallest radius value (r_2) to the

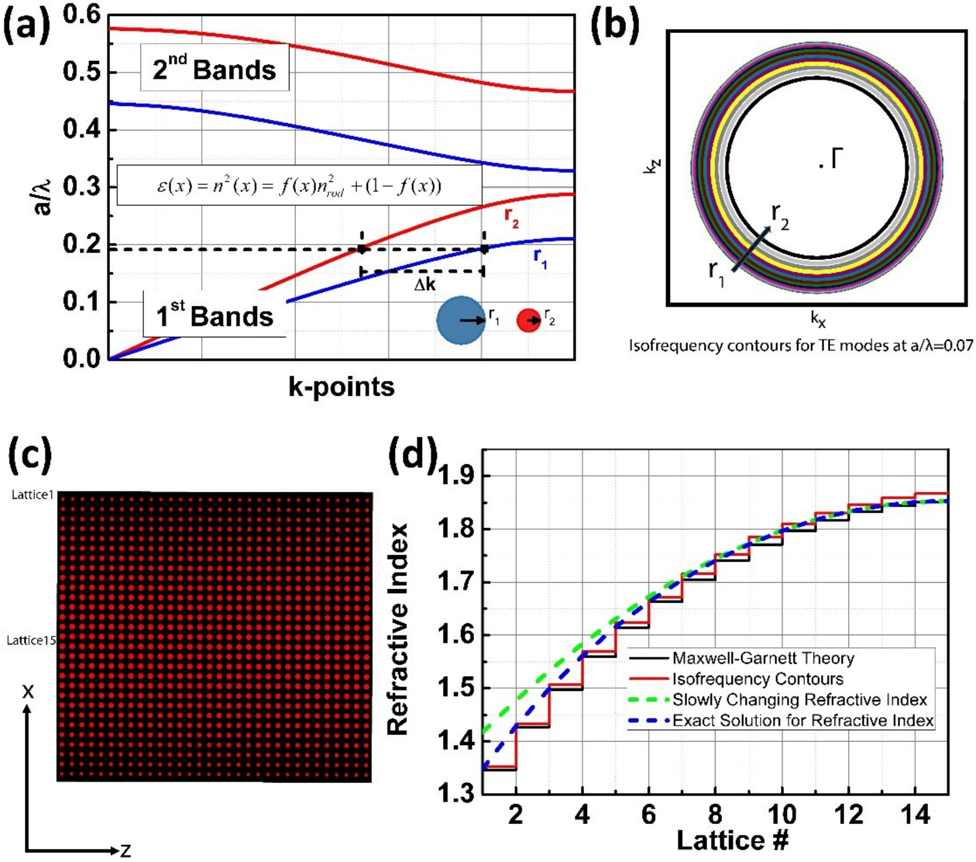

Figure 3. (a) Dispersion graph for two radius values: $r_2 = 0.3a$ (blue line) and $r_1 = 0.173a$ (red line). (b) Isofrequency contours (IFCs) calculated for each rod with different filling factors. The circular IFCs belong to the 1st band of the rod configurations again at $f = 0.07\ a/\lambda$. The smallest filling factor constitute the smallest circle in the IFC whereas the largest is plotted as the largest circle. (c) The realized GRIN PC by modifying the rod radii. (d) The refractive index evaluated at different points of the GRIN PC structure as a function of the rod number where lattice 1 corresponds to the outermost rod and vice versa. Maxwell-Garnett theory predicts the black step-wise plot at distinct lattice points for the corresponding rods, IFC calculations predict red step-wise plot, a slowly changing refractive index treatment gives the continuous homogenized GRIN medium shown in dashed green and the exact solution of the polynomial GRIN medium is shown with dashed blue curve.

largest element (r_1). It becomes hard to distinguish the larger IFCs since they get very close to each other. The centered isotropic IFCs mean that we can estimate the regarding phase velocity directly and correspondingly an effective refractive index for each lattice element. Hence, a secondary homogenized refractive index can be estimated on top of the values offered by Maxwell-Garnett theory. These values are plotted together in Fig. 3(d) as step plots for each homogenized lattice element. The consistency between these plots is evident. The small mismatches are mainly caused by the difficulty of precisely estimating the phase velocity for larger radius values.

In the end, the structure as shown in Fig. 3(c) is constructed with 29 rods along x-axis. The wave propagation will be along z-axis. The homogenized refractive index values retrieved from both Maxwell-Garnett theory and IFCs are compared with the polynomial continuous change that has the form of $n^2(x) = n_0^2(1 - \alpha^2 x^2)$. This quadratic GRIN medium is very well known in traditional GRIN optics. Most of the time, this function is expanded so that a direct estimation of the refractive index rather than the dielectric permittivity can be obtained. Then, the refractive index becomes $n(x) = n_0(1 - \alpha^2 x^2/2)$. Yet, this approximation is obviously only valid when α is very small, which is also attributed to be the slowly changing GRIN medium. In our case, the half width of the GRIN PC lens is $14a$ and the refractive index is not slowly changing. The two refractive index functions are plotted together in Fig. 3(d) for the retrieved n_0 and α values, which also clearly show that the Taylor expansion for small α cannot be applied for the current study. On the other hand, the continuous GRIN optics $n(x)$ almost perfectly agrees with the Maxwell-Garnett theory and closely follows IFC based GRIN PC homogenization efforts. Accordingly, Fermat's Eikonal equation for the shortest path of the rays in GRIN optics for the exact solution needs to be obtained. Such rays would describe how light would propagate inside the GRIN PC and alter its wavefront.

While the ray propagates from point A to B, Fermat's principle dictates that the optical path calculated needs to be at an extremum:

$$\int_A^B n(r)ds = extremum \tag{3-1}$$

where $n(r)$ is the defined refractive index along the path ds and $ds = \sqrt{dx^2 + dz^2}$ assuming that the rods are infinitely extending and the refractive index is invariant along y-axis. A very quick solution can be obtained by strictly working with paraxial waves, which states that the slope of the ray with the main optical/propagation axis is very small and the ray is almost parallel to the z-axis, in other words $ds \approx dz$ [44].

Yet, for our GRIN PC configuration we cannot assume the validity of the paraxial waves, either. The variation principle applied to Eq. (3-1) will bring $\delta\int_A^B n(r)ds = 0$. The solutions to the variation principle will be obtained with optical Euler-Lagrangian equations which give the relationship between the length covered by the ray (*s*) and the refractive index function (*n*) as shown in Eq. (3-2) [45]:

$$\frac{d}{ds}\left(n\frac{dr}{ds}\right) = \nabla n \Rightarrow \frac{d}{ds}\left(n\frac{dx}{ds}\right) = \frac{dn}{dx}, \frac{d}{ds}\left(n\frac{dz}{ds}\right) = \frac{dn}{dz} \tag{3-2}$$

Even though the refractive index in our GRIN PC is changing along *z*-axis in reality as it is seen in Fig. 3(c), the homogenization efforts simply dictate that $dn/dz = 0$ as the same type lattices are assembled in this direction, which would imply the following relationship as it is given in Eq. (3-3):

$$n(x)\frac{dz}{ds} = \frac{n(x)}{\sqrt{dx^2 + dz^2}}dz = \frac{n(x)}{\sqrt{\frac{dx^2}{dz^2} + 1}} = C_1 \tag{3-3}$$

where n is only a function of x and C_1 is a constant quantity which will give $dn/dz = 0$. A rearrangement of Eq. (3-3) can be done in order to obtain z after plugging in the exact quadratic function for $n(x)$ where a secondary constant $C_2 = \sqrt{(n_0^2 - C_1^2)/n_0^2\alpha^2}$ is introduced as the ratio of the other constants in our problem. Hence, Eq. (3-4) can predict the position of the ray along *z*-axis once the ray's initial position X_i and the final position X_f are known. Yet, most of the time we are interested in the position of the ray along *x*-axis as the propagation continues along *z*-axis:

$$z = \int_{X_i}^{X_f} \frac{C_1}{\sqrt{n(x)^2 - C_1^2}}dx = \int_{X_i}^{X_f} \frac{\frac{C_1}{n_0\alpha}}{\sqrt{\frac{n_0^2 - C_1^2}{n_0^2\alpha^2} - x^2}}dx$$
$$= \frac{\sqrt{1 - C_2^2\alpha^2}}{\alpha}\int_{X_i}^{X_f} \frac{1}{\sqrt{C_2^2 - x^2}}dx \tag{3-4}$$

Once we solve the integral given in Eq. (3-4) and try to express X_f as a function of X_i and z, we end up with Eq. (3-5):

$$X_f = C_2 sin(\frac{\alpha z}{\sqrt{1 - \alpha^2 C_2^2}} + sin^{-1}(\frac{X_i}{C_2})) \tag{3-5}$$

The second important quantity will be the slope of the ray which is defined as $tan(\theta) = dx/dz$ in our coordinate axis arrangement. In order to understand the ray propagation in our GRIN PC, we need to solve for the boundary conditions. At the input side we have waves coming at normal incidence with respect to the *x*-axis just before they penetrate into the GRIN PC, ie. θ_i=0 when *z*=0. Eq. (3-5) can be solved at the input surface to find out the constant C_2:

$$X_i = \pm C_2 \Rightarrow sin^{-1}\left(\frac{X_i}{C_2}\right) = (2n+1)\frac{\pi}{2} \tag{3-6}$$

where *n* is any integer number. The boundary condition can be applied for every different case of the impinging fields. Then, similar to the metamaterial counterpart, TMM (also called ABCD matrix for the ray optics treatment) of the GRIN PC structure can be obtained for the known input slope and position for the most general case. Eq. (3-5) can be expanded in the following form and the slope can also be retrieved:

$$\begin{gathered} X_f = C_2\left[si\,n\left(\frac{\alpha z}{\sqrt{1-\alpha^2 C_2^2}}\right) cos\left(sin^{-1}\left(\frac{X_i}{C_2}\right)\right) + cos\left(\frac{\alpha z}{\sqrt{1-\alpha^2 C_2^2}}\right)\frac{X_i}{C_2}\right] \\ tan(\theta_f) = \frac{C_2\alpha}{\sqrt{1-\alpha^2 C_2^2}}\left[cos\left(\frac{\alpha z}{\sqrt{1-\alpha^2 C_2^2}}\right) cos\left(sin^{-1}\left(\frac{X_i}{C_2}\right)\right) \right. \\ \left. - sin\left(\frac{\alpha z}{\sqrt{1-\alpha^2 C_2^2}}\right)\frac{X_i}{C_2}\right] \end{gathered} \tag{3-7}$$

However, since the boundary condition for *z*=0 will yield $tan(\theta_i)\sqrt{1-\alpha^2 C_2^2}/(\alpha C_2) = cos\left(sin^{-1}(X_i/C_2)\right)$, we can plug it into Eq. (3-7) to end up with the TMM:

$$\begin{bmatrix} X_f \\ tan(\theta_f) \end{bmatrix} = \begin{bmatrix} cos\left(\frac{\alpha z}{\sqrt{1-\alpha^2 C_2^2}}\right) & sin\left(\frac{\alpha z}{\sqrt{1-\alpha^2 C_2^2}}\right)\frac{\sqrt{1-\alpha^2 C_2^2}}{\alpha} \\ -\frac{\alpha}{\sqrt{1-\alpha^2 C_2^2}} sin\left(\frac{\alpha z}{\sqrt{1-\alpha^2 C_2^2}}\right) & cos\left(\frac{\alpha z}{\sqrt{1-\alpha^2 C_2^2}}\right) \end{bmatrix} \begin{bmatrix} X_i \\ tan(\theta_i) \end{bmatrix} \tag{3-8}$$

$$\begin{bmatrix} X_f \\ tan(\theta_f) \end{bmatrix} = \begin{bmatrix} A & B \\ C & D \end{bmatrix} \begin{bmatrix} X_i \\ tan(\theta_i) \end{bmatrix}$$

One should be cautious that the solutions highlighted in Eq. (3-3) do not impose the SELFOC gradient medium that is satisfied in Fig. 4(b) under the assumption of paraxial waves and a slowly changing refractive index. On the other hand, the ray trajectories are plotted in Fig. 4(a) for the general case. It is immediately seen that a very thick GRIN medium is required when SELFOC type lenses are built. The focusing takes place at a position drastically further away while the rays are propagating inside GRIN medium in Fig. 4(b) compared to Fig. 4(a) at the same wavelength. Another important drawback comes from the strict numerical aperture of the lens. The lens in Fig. 4(a) has a much larger width. In contrast, our GRIN PC will be prone to aberrations as the rays have different pitch lengths depending on the exact position of the entrance into the GRIN PC. A relatively blurred focusing will be achieved around $z=2\lambda$ as it can be depicted from Fig. 4(a).

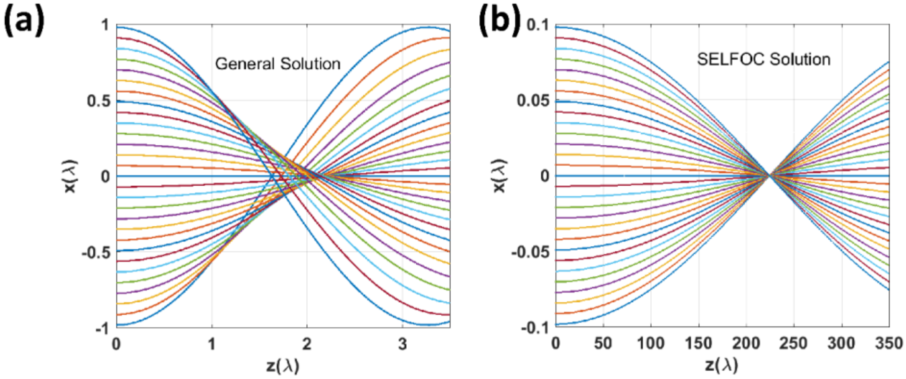

Figure 4. Ray propagation inside GRIN media for two different conditions. (a) General solution as highlighted in Eq. (3-8). (b) SELFOC solution under the assumption of paraxial rays and slowly changing refractive index.

As the focal length of the TMM given in Eq. (3-8) depends on the constant C_2, it would be a critical choice to find the most suitable thickness of the GRIN PC for focusing. In the case of a SELFOC lens, the period of the cosine function in the TMM matrix yields simply:

$$cos(\frac{\alpha L}{\sqrt{1-\alpha^2 C_2^2}}) \approx \cos(\alpha L) = 0 \Rightarrow L = \frac{\pi}{2\alpha} \tag{3-9}$$

which is the well-known periodic pitch length while $\alpha^2 C_2^2 \ll 1$. Two different thicknesses have been chosen in Fig. 5 to show the focusing phenomena solely based on ray optics. As the ray reaches the end of GRIN PC which is depicted for $\Delta z=1.75\lambda$ and 2.24λ, the refraction will determine the outgoing ray trajectory. Then, the outgoing ray angle can be written in the following way. Recognizing $n^2(X_f) = n_0^2(1-\alpha^2 X_f^2)$, $C_2 = X_i$ and $tan(\theta_i) = 0$, we obtain:

$$\begin{gathered} tan^{-1}\left(-\frac{\alpha C_2}{\sqrt{1-\alpha^2 C_2^2}} sin(\frac{\alpha \Delta z}{\sqrt{1-\alpha^2 C_2^2}})\right) = \theta_f \\ \theta_{out} = sin^{-1}\left(n_0\sqrt{1-\alpha^2 C_2^2 cos^2\left(\frac{\alpha \Delta z}{\sqrt{1-\alpha^2 C_2^2}}\right)} sin(\theta_f)\right) \end{gathered} \tag{3-10}$$

Furthermore, the outgoing angle would determine the focal point (Δf) for that particular ray as follows:

$$tan(\theta_{out}) = \frac{X_f}{\Delta f} \Rightarrow \Delta f = \frac{X_f}{tan(\theta_{out})} \tag{3-11}$$

Combining the results of Eqs. (3-10) and (3-11) would give an idea about Δf. The change in the trajectory can also be seen in Fig. 5. When $\Delta z= 2.24\lambda$, the ray is already very close to the optical axis. Nonetheless, it is very difficult to determine a single Δf for this configuration as we critically witness the aberration in Fig. 4(a), as well. As a result, the determination of the most suitable Δf value requires implementation of wave optics and Finite Difference Time Domain (FDTD) based results to be utilized.

3.2. Wave Optics: Focusing and Source Dependent Propagation under Gaussian beam illumination

Ray optics relies on the fact that $\lambda \rightarrow 0$ whereas Maxwell-Garnett effective medium theory is valid in the long wavelength, namely the metamaterial regime $\lambda \gg a$. These two requirements will bring in differences between the short-wavelength ray optics and long-wavelength metamaterial assumptions. Ray optics still offer an insight regarding the preliminary design of the GRIN PCs but wave optics based solutions are needed to overcome the limits of the ray optics.

Hence, GRIN PCs that are Δz=1.75λ and 2.24λ long have been chosen with Δx=2λ width. A Gaussian beam source illuminates the input side with almost normal incidence. FDTD based solutions are given in Fig. 6. The real part of the transverse electric field (Re{E_y}) has been plotted in Fig. 6(a) and (b) in order to explicitly show the phase retardation mechanism that creates the focusing effect. The intensity plots clearly show that the focusing occurs at the exit side of the GRIN PC. Interestingly, the thicker GRIN PC on the right has a longer Δf compared to the shorter GRIN PC. This is consistent with previous results reported in ref. 46 where a secant hyperbolic GRIN PC was investigated. Yet, it would not be predictable solely based on Eq. (3-11). Furthermore, the thicker GRIN PC has a better impedance matching to the incoming beam such that it can channel more energy to the output side.

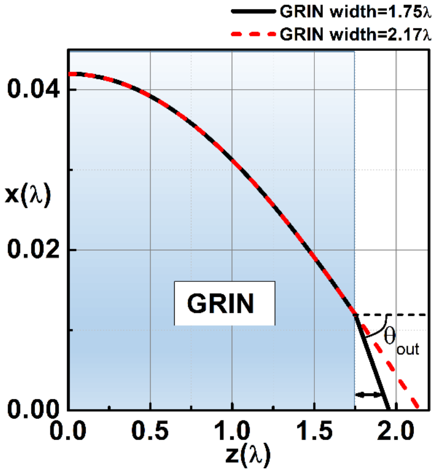

Figure 5. Ray trajectories when GRIN has a thickness of Δz=1.75λ (black solid curve) and 2.24λ (dashed red curve).

The illumination by a Gaussian beam brings in differences when compared to ray optics and also plane waves. Such effects are covered in depth for GRIN optics. One of the first trivial mismatch occurs in the Δf. This shift between different illumination sources is analytically shown in ref. 23 Ch. 4 under paraxial and slowly changing refractive index assumptions for a quadratic GRIN medium. Figure 7 shows two cases with uniform (plane wave) and Gaussian-type illuminations. Periodic boundary conditions have been assumed for the plane wave excitation. FDTD solutions also demonstrate the imaging and focusing differences, which depend on the illumination sources. As expected, the realistic Gaussian beam type illumination creates a waist at the output while the working distance (Δf) has now more depth. The Gaussian beam can be focused over a slightly longer depth along z-axis, which is expressed as the quality of the depth of focus (DOF) for lenses. In other words, the depth of focus of the lens is improved by sacrificing from the resolution under Gaussian beam type illumination. We can conclude that such phenomena that were observed in GRIN optics are also valid for our GRIN PC structure.

Another overlooked property of the GRIN PC is the source size for the Gaussian type illuminations. A Gaussian beam does not automatically yield lensing in GRIN PC structures. The beam interaction depends heavily on the width (w) of the

Gaussian beam. Figure 8 depicts 4 different cases with varying w. Ref. 23 explains that the GRIN optics have Hermite-Gaussian eigenmodes and the incoming wave would be coupled into such modes. The half-width of the fundamental mode is defined as w_{fm}. In case $w_{fm}=w/2$ at the GRIN medium's entrance, the mode would be an adiffractional Gaussian beam and would propagate as the fundamental mode. We clearly see a very similar phenomenon happening in Fig. 8. The beam diverges for Fig. 8(a) and we can label this case as $w<w_{fm}$. On the other hand, Figs. 8(c) and (d)

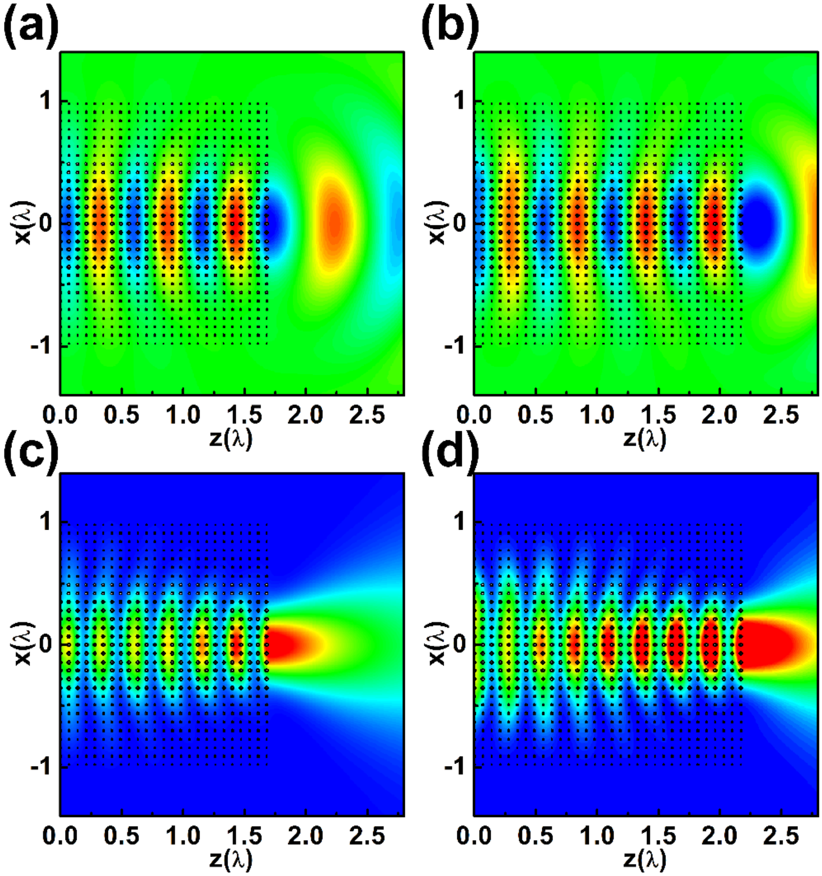

Figure 6. Electric field (E_y) spatial distributions from FDTD results at $f = 0.07\ a/\lambda$. The GRIN PC has been highlighted with black circles for each case. (a) Re$\{E_y\}$ and (c) $|E_y|^2$ when Δz=1.75λ, (b) Re$\{E_y\}$ and (d) $|E_y|^2$ when Δz=2.24λ. The source is a Gaussian beam with a width of 1.14λ. The plots are normalized with respect to the unit intensity.

show the lensing characteristics when $w_{fm}<w$. The adiffractional propagation almost occurs in Fig. 8(b). We would conclude that a very similar assessment of the Gaussian beam propagation is also valid for our GRIN PC.

3.3. Imaging and Fourier Transform with GRIN PC

In order to understand the imaging characteristics of the GRIN PC lens, a current source infinitely extending along y-axis is placed at x=-0.56λ at the input side of the

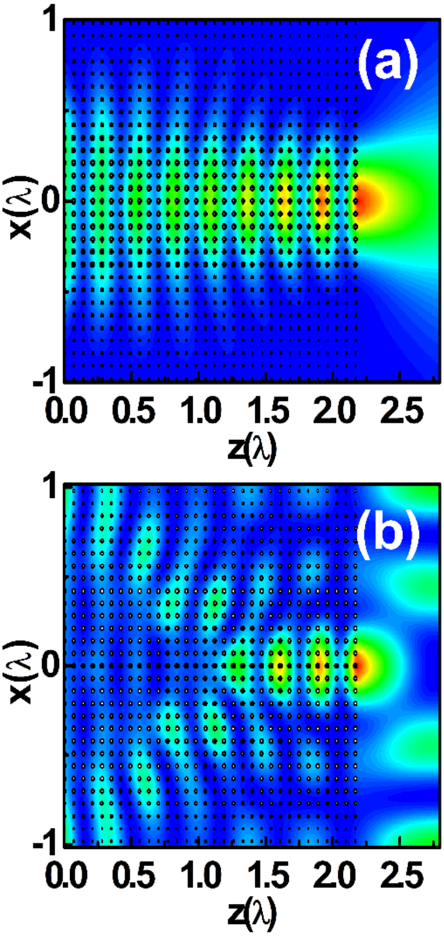

Figure 7. Spatial distributions of the intensity ($|E_y|^2$) when Δz=2.24λ from FDTD results at $f = 0.07\ a/\lambda$. The GRIN PC has been highlighted with black circles for each case. (a) Gaussian beam type illumination with a width of 1.14λ and (b) Plane wave (uniform) illumination. The plots are normalized with respect to their maximum intensity values. The same intensity distribution in Fig. 6(d) is replotted in (a) with a different normalization in order to study the impact of the illumination sources.

lens. The current source sits 0.14λ away from the lens. The created image of any lens at the output side is expected to take a double Fourier Transform in the form of:

$$\boldsymbol{\mathcal{F}}\{\boldsymbol{\mathcal{F}}\{f(x)\}\} = f(-x) \tag{3-12}$$

where $\boldsymbol{\mathcal{F}}$ stands for Fourier Transform and *f*(*x*) is the image at the input side. Hence, the image would be inverted. This is also seen in Fig. 9 as the image is created on the +*x* side. The image is created 0.23λ away from the lens at the output side. The aberration problems caused by the astigmatism of the GRIN PC is evident during the image formation. The ray optics treatment in Fig. 4(a) already gave clues about this aberration problem for this particular GRIN PC, which is not considered to be a traditional SELFOC medium. The peak of the intensity at the exit side is formed at x=0.6λ, which is very close to the location of the current source at the input side.

The GRIN optics elements are characterized with kernel (point spread) functions. The kernel function ($K(x,x_0;z)$) would be used to form the images at the output side. For the SELFOC media, a canonical integral transformation is used:

$$\Psi(x;z) = \int \Psi(x_0; z=0) K(x_0, x; z) dx_0 \tag{3-13}$$

Eq. (3-13) images the field at the input transversal plane $\psi(x_0;z=0)$ to the output transversal plane $\psi(x;z)$. Since imaging systems are linear systems, the kernel function would define the impulse response of the system. For the slowly changing refractive index condition, the kernel function is derived to be in the following format in ref. 23:

$$K(x_0, x; z) = \frac{k_0 n_0 \exp(ik_0 n_0 z)}{i2\pi B(x,z)} \times exp\left\{\frac{-k_0 n_0}{i2B(x,z)}[A(x,z)x_0^2 + D(x,z)x - 2xx_0]\right\} \tag{3-14}$$

where A, B and D are the TMM 2x2 matrix parameters illustrated in Eq. (3-8) and k_0 and n_0 are the free space wave vector and the refractive index at the center of the GRIN medium, respectively. For the SELFOC medium ($\alpha^2 C_2^2 \ll 1$) at $z = L = \pi/2\alpha$, both A and D would become zero while $B = \sin(\alpha L)/\alpha = 2L/\pi$ as Eq. (3-9) also implies. Under these conditions, Eq. (3-13) can be rewritten as:

$$\Psi(x;z) = \frac{k_0 n_0 \exp(ik_0 n_0 z)}{i4L} \int \Psi(x_0; z=0) exp\left\{\frac{-i2\pi x x_0 k_0 n_0}{4L}\right\} dx_0 \tag{3-15}$$

$$= \mathcal{F}\{\Psi(x_0; z = 0)\}$$

which is the Fourier Transform of the input wave. This condition is very much similar to the propagation through the standard lens. Now, we need to assign the spatial frequency for this lensing scenario. The spatial frequency is $v_x = \pi x n_0 / 2\lambda L$ as opposed to $v_x = x/\lambda L$ in standard lensing.

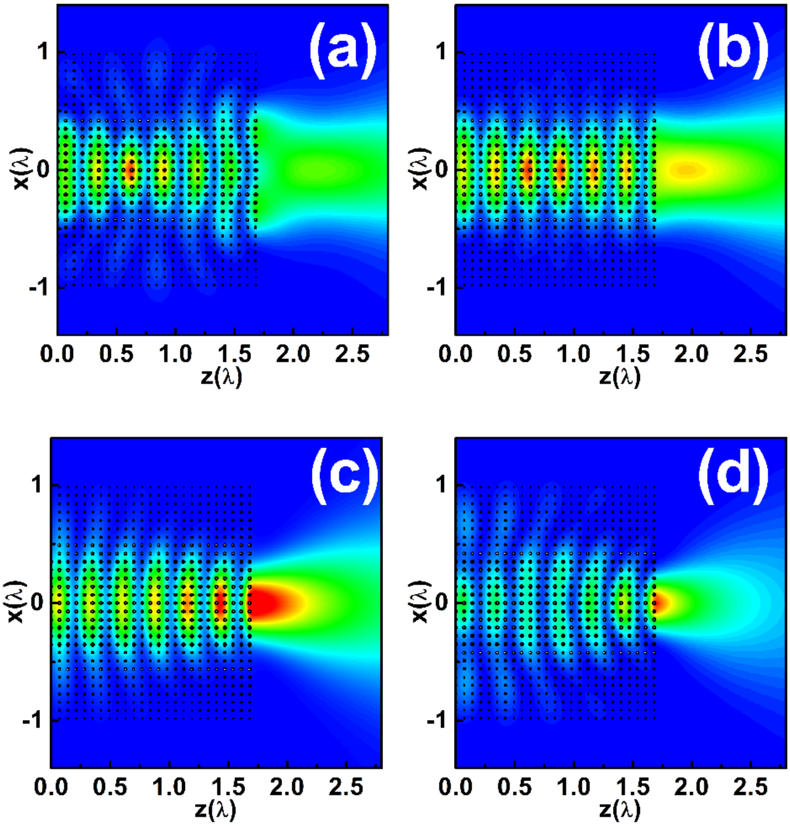

Figure 8. Spatial distributions of the intensity ($|E_y|^2$) when Δz=1.75λ from FDTD results at $f = 0.07\ a/\lambda$ under Gaussian beam type illumination for different beam widths. The GRIN PC has been highlighted with black circles for each case. Gaussian beam source has a width of (a) w=0.38λ, (b) w=0.76λ, (c) w=1.14λ and (d) w=1.52λ. The plots are normalized with respect to their maximum intensity values. The same intensity distribution in Fig. 6(c) is replotted in (c) with a different normalization in order to study the impact of the width of the Gaussian beam type sources.

The validity of Eq. (3-15) for our GRIN PC which is not a SELFOC medium will be tested. If we stick with the same kernel function, both A and D become very small when GRIN PC is Δz=2.24λ and B is almost $1/\alpha$. However, we also have the finite aperture of the lens that we need to take into consideration. This aperture (w_{ap}) function will determine the resolution of the lens since the GRIN medium is not infinite. The aperture can be modelled with a $rect(x/w_{ap})$ function as follows:

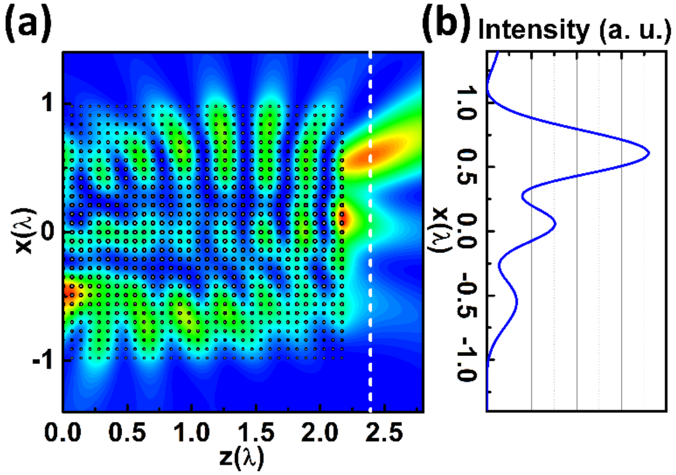

Figure 9. (a) Spatial distribution of the intensity ($|E_y|^2$) when Δz=2.24λ from FDTD results at $f = 0.07a/\lambda$. A dipole source is located at the input side (x=-0.56λ, z=-0.14λ) of the GRIN PC and image is formed at the exit side (x=+0.6λ, z=2.4λ) to understand the imaging characteristics. (b) The intensity distribution at z=2.4λ is plotted.

$$rect\left(\frac{x}{w_{ap}}\right) = \begin{cases} 1, |x| \leq w_{ap}/2 \\ 0, |x| > w_{ap}/2 \end{cases} \tag{3-16}$$

Then, simply if an input function $\psi_{test}(x_0, z=0)$ is launched towards the GRIN PC, the wavefunction at the input side of the transversal plane of the GRIN PC will be the multiplication of the test function with the aperture function. Hence, Eq. (3-15) will become:

$$\Psi_{out} = \frac{k_0 n_0}{i4L} \exp(ik_0 n_0 z) \int \Psi_{test}(x_0) rect(\frac{x_0}{w_{ap}}) exp\left\{\frac{-i2\pi x x_0 k_0 n_0}{4L}\right\} dx_0 \tag{3-17}$$

$$\Psi_{out} = \boldsymbol{\mathcal{F}}\{\Psi_{test}(x_0)\} \otimes \boldsymbol{\mathcal{F}}\left\{rect(\frac{x_0}{w_{ap}})\right\}$$

as convolution theorem suggests once we drop the constant phase term ($\exp(ik_0 n_0 z)$) in front. Figure 10 shows the case when we feed the GRIN PC with a Gaussian test function of the form $\Psi_{test}(x_0) = \exp(-4x_0^2/w_g^2)$ where $w_g \approx 1.52\lambda$ is the full waist of the Gaussian and $w_{ap} \approx 2.03\lambda$. Hence, Eq. (3-17) will turn into:

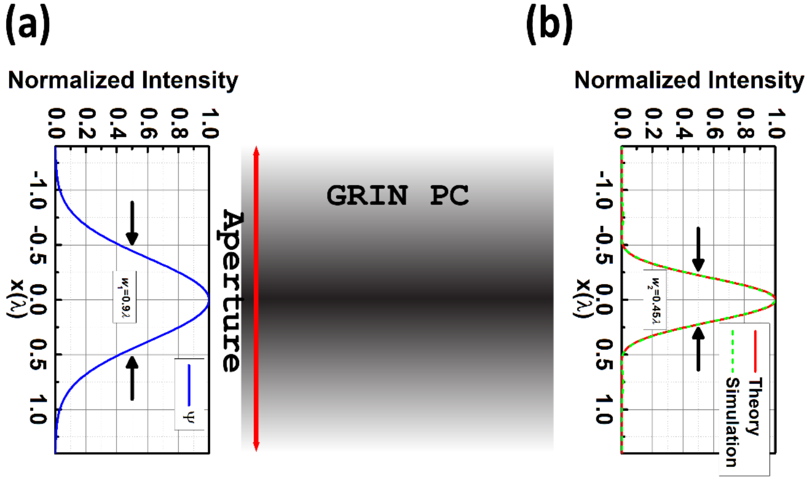

Figure 10. Fourier Transform capability of the GRIN PC with the applied test function. (a) The normalized intensity distribution of a Gaussian test function at the input of the GRIN PC. The width of the test Gaussian function is 0.9λ. (b) The normalized intensity distribution at the output of the GRIN PC (dashed green curve) as the FDTD simulation results offer at $f = 0.07a/\lambda$ and Δz=2.24λ. The result of the normalized intensity distribution (solid red curve) at the output based on Eq. (3-17). The width of the output wavefunction decreases from w_1=0.9λ to w_2=0.45λ.

$$\mathcal{F}\left\{rect(\frac{x_0}{w_{ap}})\right\} = \frac{\sin(\pi w_{ap} v_x)}{\pi v_x}\sqrt{\frac{k_0 n_0}{i4L}} \tag{3-18}$$

$$\mathcal{F}\{\Psi_{test}(x_0)\} = \frac{\sqrt{\pi}}{2} w_g exp\left(\frac{-\pi^2 w_g^2 v_x^2}{4}\right)\sqrt{\frac{k_0 n_0}{i4L}}$$

The resulting wavefunction at the exit side has been plotted together with the FDTD based simulation results in Fig. 10(b). The results suggest that even though our GRIN PC is not a SELFOC medium, the kernel and canonical integral transformation do yield very similar results to the SELFOC versions. The GRIN PC narrows down the width of the outgoing beam from 0.9λ to 0.45λ. The fact that Fourier transforming capability of the lens is valid has already been already backed up by the previously discussed focusing cases related to FDTD based results in Figs. 6-8, even without the presence of a SELFOC medium.

Finally, the Fractional Fourier Transform capability of the GRIN PC is tested in a similar fashion. GRIN optics dictate that the modes inside the GRIN medium propagate in such a way that would naturally realize Fractional Fourier Transform. GRIN medium provides the Fractional Fourier Transform in its purest simplest form [47]. Then, the kernel function would be modified such that $\alpha L < \pi/2$ for the SELFOC medium as the self-focusing distance has not been reached yet. Accordingly, a fractional scaling factor can be defined for the SELFOC and adapted for our GRIN PC:

$$\beta = \frac{\alpha L}{\pi/2} \Rightarrow \frac{\dfrac{\alpha \Delta z}{\sqrt{1-\alpha^2 C_2^2}}}{\pi/2} \tag{3-19}$$

This modification brings in the fact that depending on the C_2 value, similar but different β values could be proposed. As it can be seen in Fig. 11(a), a GRIN PC that is much shorter, Δz=1.05λ is selected and the fields are collected at the output of the GRIN PC. Unlike the treatment of a homogenous GRIN medium, the near-field interactions make this process quite tricky together with the impedance mismatch at the air-GRIN PC interface. The field should be obtained not from the air but as close as possible to the GRIN PC as we are interested in the natural Fractional Fourier Transform of the GRIN PC. The simulation result is plotted in Fig. 11(b) together with the results based on Fractional Fourier Transform for two possible β values. The preliminary results suggest that Fractional Fourier Transform capability can also be addressed with GRIN PC that is not a SELFOC medium, itself. When Δz=1.05λ, β value ranges between 0.4 and 0.43 based on Eq. (3-19) for different ray trajectories depicted in Fig. 4(a).

A frequency sweep shows that the dielectric lenses are much more suitable for larger bandwidth applications, as depicted in Fig. 12. Two higher frequencies were selected as $a/\lambda = 0.1167$ and $a/\lambda = 0.2$. These two frequencies still reside in the first band of the dielectric rods, which is shown in Fig. 3(a). Maxwell-Garnett theory based homogenization is frequency independent. Nevertheless, it presents very consistent results for $a/\lambda = 0.07$. As we move up close to $a/\lambda = 0.2$, Maxwell-Garnett homogenization method results will deviate from what IFCs present. IFCs will still be circular centered around Γ point, resembling Fig. 3(b). Yet, the actual refractive index of each lattice will be different from Maxwell-Garnett's predictions. The refractive index gradual change can still be expressed with a quadratic relationship (with some tolerable deviation). However, α value will be different than what has been assumed throughout the paper for $a/\lambda = 0.07$. A quick analysis shows that α will need to increase as the refractive index change becomes more pronounced over each lattice in the transverse direction while frequency of operation is increasing. On the other hand, the ray optics assumptions will be more suitable for these higher frequencies. Eq. (3-9) will dictate that a shorter lens is required for focusing. Figure 12 also illustrates that focusing condition has been already met before the waves reach the full width. Nevertheless, Fig. 12(a) still offer focusing at the exit side of the GRIN PC, which can also be claimed for Fig. 12(b). There is a competing phenomenon coming into play for Fig. 12(b), which is the traditional Bragg interactions of the wave with the periodic crystal. As the wavelength is decreased, the wave starts to actually “see” each scatterer instead of a homogenous medium and the peculiar wavefront formations are observed as in the case of Fig. 12(b). Shortly, since the change in α is not very large compared to the originally studied case in $a/\lambda = 0.07$, the same GRIN PC length could be used for both cases in Fig. 12. Once the focusing is achieved and the modified Gaussian beam reaches its shortest

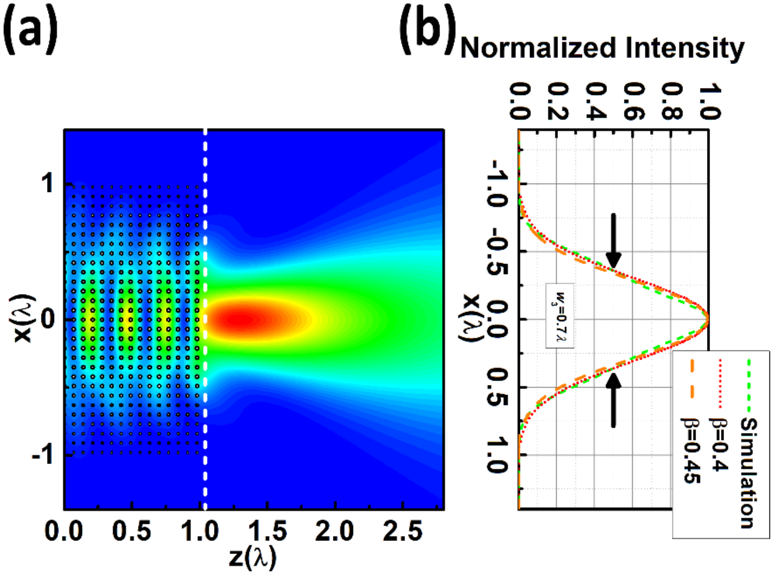

Figure 11. Fractional Fourier Transform capability of the GRIN PC with the applied test function. (a) Spatial distribution of the intensity ($|E_y|^2$) when Δz=1.05λ from FDTD results at $f = 0.07\ a/\lambda$. The same Gaussian test function also with the same width as in Fig. 10 is applied at the input of the GRIN. (b) The normalized intensity distribution of the output of the GRIN PC (dashed green curve) as the FDTD simulation results offer at the output of the GRIN PC (at the dashed white line). The result of the normalized intensity distribution at the output based on Fractional Fourier Transform for β=0.4 (dotted red curve) and β=0.45 (dashed orange curve). The width of the output wavefunction decreases from w_1=0.9λ to w_2=0.7λ.

waist inside the GRIN PC, it starts diverging in Fig. 12(b) more significantly. The bandwidth of the lens is limited by the Bragg interactions rather than by the bandgap. The GRIN PC still offers much better performance than the metallic, resonance analogs that are shown in Fig. 2. Lastly, the same physical size of the Gaussian beams that have been used in the original case has been launched in Fig. 12. Since, $w_{fm}<w$ at the largest wavelength ($a/\lambda = 0.07$), the shorter wavelength cases would already force the beam to focus.

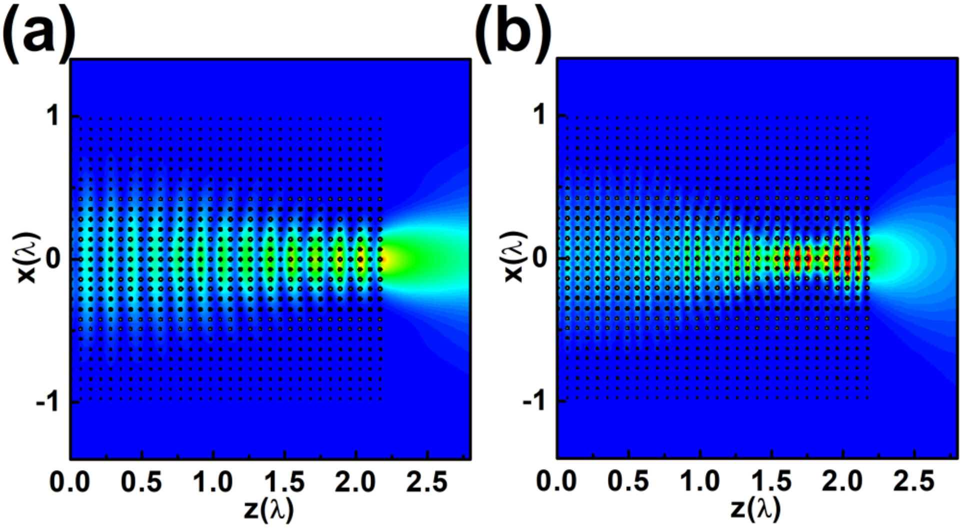

Figure 12. Spatial distribution of the intensity ($|E_y|^2$) when Δz=2.24λ from FDTD results at (a) $f = 0.1167a/\lambda$ and (b) $f = 0.2a/\lambda$. The source is a Gaussian beam with a fixed width used in Fig. 6(d). The normalization has been carried out with respect to the highest intensity values for each frequency.

4. CONCLUSION

In conclusion, a GRIN PC medium which has not been traditionally investigated because of its abrupt refractive index distribution is studied in details. The studied GRIN PC is shown to behave in very close correlation to its slowly perturbed refractive index possessing GRIN counterparts at its core physics. Concepts from GRIN optics have been borrowed to explain the ray trajectories, wave optics phenomena together with imaging and Fourier optics in such untraditional GRIN PCs to be used as lenses with wide numerical apertures and relatively much shorter lengths over a considerably large bandwidth.

The analysis has started by discussing and comparing GRIN PCs with volumetric MTMs. The resonance nature and the impedance matching difficulties of the MTMs have been highlighted as the main factors which directed the researchers to switch to GRIN optics. The ray trajectory of the studied GRIN PC has been derived, which also pointed out the ABCD matrix for this untraditional GRIN PC design. The wave nature of the current GRIN PC design has been investigated under the light of the derived ABCD matrix. The simulations have shown that the imaging capabilities of a point source can easily be demonstrated for the current GRIN PC. Since the current GRIN PC can perform imaging by taking the double Fourier Transform of a point source, a kernel function adapted from the GRIN optics has been applied to understand the single Fourier Transform capability. The presented results have illustrated that the impulse response which is valid for the SELFOC GRIN medium can be utilized and the present GRIN PC can take the Fourier Transform of a test Gaussian function. Moreover, the Fractional Fourier Transform of the test Gaussian function is also verified at the output of the GRIN PC.

The bandwidth is shown to be limited by the emergence of the Bragg interactions of the wave with the periodic scatterers. A seemingly ambiguous GRIN PC, such as the one currently studied that does not possess an easy analytical solution without the paraxial approximation and a large refractive index variance, has not been studied extensively in the literature. The present work shows that even such a GRIN PC can exhibit not only very similar Fourier Transforming capabilities but also Fractional Fourier Transform properties as one would expect to see in GRIN optics. The adiffractional beam propagation is shown with the careful selection of the excitation sources. The adifractional beam propagation is very critical at the end of fiber optic waveguides where the beam tends to quickly diverge and a small portion of the wave information can be transmitted to the next optical device. The present design with its high numerical aperture can be used to collimate the light as an output coupler in a real life application. The characteristics of such an output coupler will be studied in a future work. Furthermore, the current design is a member of the broad research family of transformation optics. The gradient filling factor has been employed to show how light can be focused in this study but similar transformational optics designs could also be analyzed from the perspective of wave impedance matching and a cloaking scheme can be implemented. The refractive index can be gradually remodulated to facilitate the cloaking by limiting the interaction of the incident light with the emerging beam. Moreover, the imaging capability of the GRIN PC can be utilized for advanced optical lithography. Exemplary application fields can be listed for the current design aside from being merely used as an imaging component. Another very useful implementation would be to utilize the current design as a fast Fractional Fourier Transform calculator. The Fractional Fourier

Transform could be calculated at the speed of light, which would be a promising improvement on top of the present methods relying on the computational power of electronics.

REFERENCES

[1] J.B. Pendry, Negative Refraction Makes a Perfect Lens, *Phys. Rev. Lett.*, 85/18 (2000) 3966–3969.

[2] D.R. Smith, J.B. Pendry and M.C.K. Wiltshire, Metamaterials and Negative Refractive Index, *Science*, 305/5685 (2004) 788-792.

[3] A. Grbic and G.V. Eleftheriades, Subwavelength focusing using a negative-refractive-index transmission line lens, *IEEE Antennas Wirel. Propag. Lett.*, 2 (2003) 186-189.

[4] K. Aydin, I. Bulu and E. Ozbay, Subwavelength resolution with a negative-index metamaterial superlens, *Appl. Phys. Lett.*, 90 (2007) 254102.

[5] D. Schurig, J.J. Mock, B.J. Justice, S.A. Cummer, J.B. Pendry, A.F. Starr and D.R. Smith, Metamaterial Electromagnetic Cloak at Microwave Frequencies, *Science*, 314/5801 (2006) 977-980.

[6] R. Liu, C. Ji, J.J. Mock, J.Y. Chin, T.J. Cui, D.R. Smith, Broadband Ground-Plane Cloak, *Science*, 323/5912 (2009) 366-369.

[7] D. Sell, J. Yang, E.W. Wang, T. Phan, S. Doshay and J.A. Fan, Ultra-High-Efficiency Anomalous Refraction with Dielectric Metasurfaces, *ACS Photonics*, 5/6 (2018) 2402-2407.

[8] C. Argyropoulos, N.M. Estakhri, F. Monticone and A. Alù, Negative refraction, gain and nonlinear effects in hyperbolic metamaterials, *Opt. Express*, 21 (2013) 15037-15047.

[9] W. Liang, Z. Li, Y. Wang, W. Chen and Z. Li, All-angle optical switch based on the zero reflection effect of graphene–dielectric hyperbolic metamaterials, *Photon. Res.*, 7 (2019) 318-324.

[10] J. Noonan and T.G. Mackay, On electromagnetic surface waves supported by an isotropic chiral material, *Opt. Commun.*, 434 (2019) 224-229.

[11] T. Gric and O. Hess, Disorder in Metamaterials Chapter 12, Advanced Thermoelectric Materials (editted by C.R. Park), (John Wiley & Sons, Inc., 2019)

[12]M. Takeda, A. Tsuchiyama, M. Okada, S. Matsui, T. Inoue and K. Aizawa, Improvement of focusing characteristics of a surface plasmonic lens for UV wavelength, *Jpn. J. Appl. Phys.*, 56 (2017) 09NC02.

[13] W.T. Chen, A.Y. Zhu, V. Sanjeev, M. Khorasaninejad, Z. Shi, E. Lee, F. Capasso, A broadband achromatic metalens for focusing
and imaging in the visible, *Nat. Nanotechnol.*, 13 (2018) 220−226.

[14] N. Kundtz and D.R. Smith, Extreme-angle broadband metamaterial lens, *Nat. Mater.*, 9 (2010) 129–132.

[15] H. Kurt and D.S. Citrin, Graded index photonic crystals, *Opt. Express*, 15 (2007) 1240-1253.

[16] D. Schurig, J.B. Pendry and D.R. Smith, Calculation of material properties and ray tracing in transformation media, *Opt. Express*, 14 (2006) 9794-9804.

[17] A.O. Cakmak, E. Colak, H. Caglayan, H. Kurt and E. Ozbay, High efficiency of graded index photonic crystal as an input coupler, *J. Appl. Phys.*, 105/10 (2009) 103708.

[18] A.E. Serebryannikov, A.O. Cakmak, E. Colak, H. Caglayan, H. Kurt and E. Ozbay, Multiple slow waves and relevant transverse transmission and confinement in chirped photonic crystals, *Opt. Express*, 22 (2014) 21806-21819.

[19] M. Gumus, I.H. Giden and H. Kurt, Broadband self-collimation in C2 symmetric photonic crystals, *Opt. Lett.*, 43/11 (2018) 2555-2558.

[20] D. Luo, G. Alagappan, X.W. Sun, Z. Raszewski and J.P. Ning, Superbending effect in two-dimensional graded photonic crystals, *Opt. Commun.*, 282/2 (2009) 329–332.

[21]E. Centeno, D. Cassagne and J.-P. Albert, Mirage and superbending effect in two dimensional graded photonic crystals, *Phys. Rev. B*, 73/23 (2006) 235119–235123.

[22] E. Akmansoy, E. Centeno, K. Vynck, D. Cassagne and J. M. Lourtioz, Graded photonic crystals curve the flow of light: An experimental demonstration by the mirage effect, Appl. Phys. Lett. 92(13), 133501 (2008).

[23] C. Gomez-Reino, M.V. Perez and C. Bao, Gradient-Index Optics: Fundamentals and Applications (Springer, 2002).

[24] P. Markos and C. M. Soukoulis, Wave Propagation From Electrons to Photonic Crystals and Left-Handed Materials, (New Jersey, Princeton University Press, 2008).

[25] G. Lubkowski, R. Schuhmann and T. Weiland, Extraction of Effective Metamaterial Parameters by Parameter Fitting of Dispersive Models, *Microw. Opt. Technol. Lett.*, 49 (2007) 285-288.

[26] B.D.F. Casse, W.T. Lu, Y.J. Huang and S. Sridhar, Nano-optical microlens with ultrashort focal length using negative refraction, *Appl. Phys. Lett.*, 93 (2008) 053111.

[27] C. G. Parazzoli, R.B. Greegor, J.A. Nielsen, M.A. Thompson, K. Li, A.M. Vetter, M.H. Tanielian and D.C. Vier, Performance of a negative index of refraction lens, *Appl. Phys. Lett.*, 84 (2004) 3232-3234.

[28] T. Driscoll, D.N. Basov, A.F. Starr, P.M. Rye, S. Nemat-Nasser, D. Schurig and D.R. Smith, Freespace microwave focusing by a negative-index gradient lens, *Appl. Phys. Lett.*, 88 (2006) 081101.

[29] R.B. Greegor, C.G. Parazzoli, J.A. Nielsen, M.A. Thompson, M.H. Tanielian and D.R. Smith, Simulation and testing of a graded negative index of refraction lens, *Appl. Phys. Lett.*, 87 (2005) 091114.

[30] D. R. Smith, J. J. Mock, A. F. Starr and D. Schurig, Gradient index metamaterials, *Phys. Rev. E*, 71 (2005) 36609.

[31] O. Paul, B. Reinhard, B. Krolla, R. Beigang and M. Rahm, Gradient index metamaterial based on slot elements, *Appl. Phys. Lett.*, 96 (2010) 241110.

[32] R. Liu, X. M. Yang, J. G. Gollub, J. J. Mock, T. J. Cui and D. R. Smith, Gradient index circuit by waveguided metamaterials, *Appl. Phys. Lett.*, 94 (2009) 073506.

[33] R. Liu, Q. Cheng, J. Y. Chin, J. J. Mock, T. J. Cui and D. R. Smith, Broadband gradient index microwave quasi-optical elements based on non-resonant metamaterials, *Opt. Express*, 17 (2009) 21030-21041.

[34] U. Levy, M. Nezhad, H.-C. Kim, C.-H. Tsai, L. Pang and Y. Fainmann, Implementation of a graded-index medium by use of subwavelength structures with graded fill factor, *J. Opt. Soc. Am. A*, 22 (2005) 724-733 (2005).

[35] U. Levy, M. Abashin, K. Ikeda, A. Krishnamoorthy, J. Cunningham and Y. Fainman, Inhomogenous Dielectric Metamaterials with Space-Variant Polarizability, *Phys. Rev. Lett.*, 98 (2007) 243901.

[36] M. Lu, B.K. Juluri, S.-C.S. Lin, B. Kirally, T. Gao and T.J. Huang, Beam aperture modifier and beam deflector using graded-index photonic crystals, *J. Appl. Phys.*, 108 (2010) 103505.

[37] H.-W. Wang and L.-W. Chen, High transmission efficiency of arbitrary waveguide bends formed by graded index photonic crystals, *J. Opt. Soc. Am. B*, 28 (2011) 2098-2104.

[38] H.-W. Wang and L.-W. Chen, A cylindrical optical black hole using graded index photonic crystals, *J. Appl. Phys.*, 109 (2011) 103104.

[39] M. Yin, X.Y. Tian, H.X. Han and D.C. Li, Free-space carpet-cloak based on gradient index photonic crystals in metamaterial regime, *Appl. Phys. Lett.*, 100 (2012) 124101.

[40] B. Vasic, G. Isic, R. Gajic and K. Hingerl, Controlling electromagnetic fields with graded photonic crystals in metamaterial regime, *Opt. Express*, 18 (2010) 20321-20333.

[41] Z.L. Mei, J. Bai and T.J. Cui, Gradient index metamaterials realized by drilling hole arrays, *J. Phys. D: Appl. Phys.*, 43 (2010) 055404.

[42] B. Vasic, R. Gajic and K. Hingerl, Graded photonic crystals for implementation of gradient refractive index media, *J. Nanophoton.*, 5 (2011) 051806.

[43] B. Vasic and R. Gajic, Self-focusing media using graded photonic crystals: Focusing, Fourier transforming and imaging, directive emission and directional cloaking, *J. Appl. Phys.*, 110 (2011) 053103.

[44] B. Saleh and M. Teich, Fundamentals of photonics (New York, Wiley, 1991).

[45] R. Weinstock, Calculus of Variations with Applications to Physics and Engineering (New York: Dover Publications, 1974).

[46] M. Turduev, I.H. Giden and H. Kurt, Design of flat lens-like graded index medium by photonic crystals: Exploring both low and high frequency regimes, *Opt. Comm.*, 339 (2015) 22-33.

[47] H.M. Ozaktas and D. Mendlovic, Fractional Fourier optics, *J. Opt. Soc. Am. A*, 12 (1995) 743-751.

Current Address: Evrim COLAK: Electrical and Electronics Engineering Department Ankara University, TURKEY
E-mail : evrim.colak@ankara.edu.tr
Orcid ID: https://orcid.org/ 0000-0002-4961-5060

Current Address: Atilla Ozgur CAKMAK: Engineering Science and Mechanics Department The Pennsylvania State University, USA
E-mail: aozgur@psu.edu
Orcid ID: https://orcid.org/ 0000-0002-3933-3203